Appendix

Chapter 3

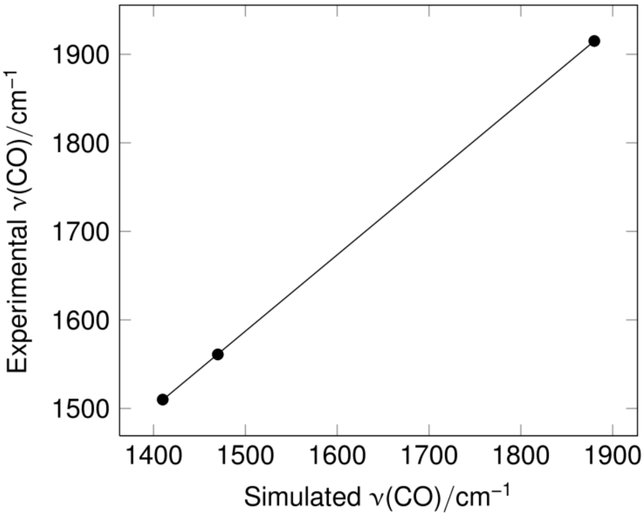

Figure A3.1 Comparison of experimental and simulated IR stretching frequencies for $[MoH_2(\eta^2\text{-}O_2CCH_3)(\text{bi-dentate phosphine})_2]^+$ complexes.

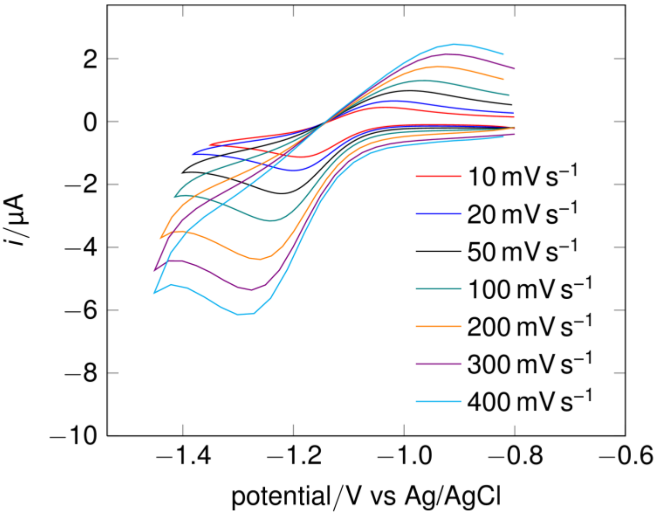

Figure A3.2 Cyclic voltammetry of 1.12 mM $[MoH_2(\eta^2\text{-}O_2CCH_3)(dppe)_2][BPh_4]$ complex in 3:1 $[NBu_4][BF_4]$-Toluene at a vitreous carbon electrode at various scan rates at 303 K.

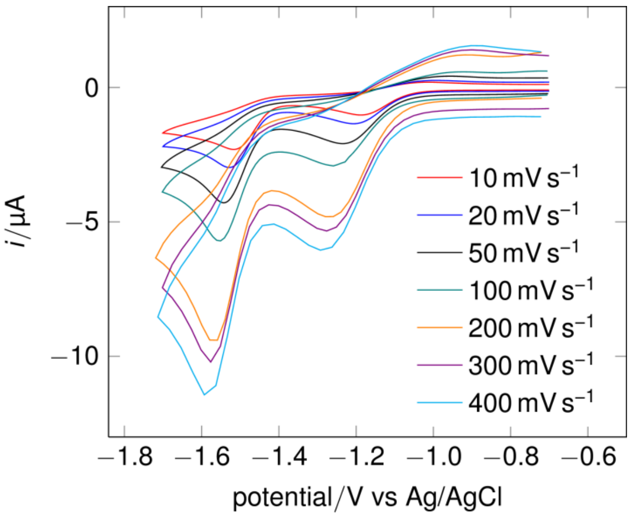

Figure A3.3 Cyclic voltammetry of 1.12 mM $[MoH_2(\eta^2\text{-}O_2CCH_3)(dppe)_2][BPh_4]$ complex in 3:1 $[NBu_4][BF_4]$-Toluene at a vitreous carbon electrode at various scan rates at 303 K.

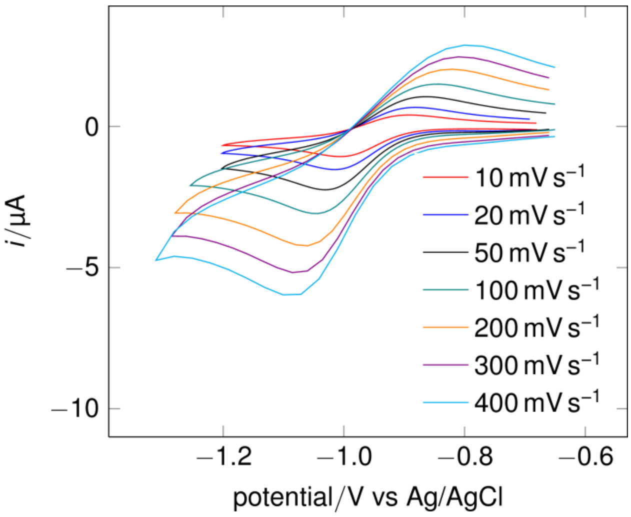

Figure A3.4 Cyclic voltammetry of 1.11 mM $[MoH_2(\eta^2\text{-}O_2CH)(dppe)_2][BPh_4]$ complex in 3:1 $[NBu_4][BF_4]$-Toluene at a vitreous carbon electrode at various scan rates at 303 K.

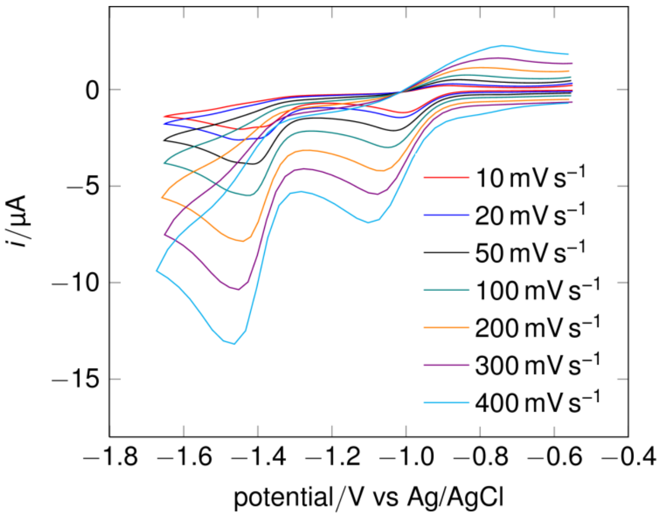

Figure A3.5 Cyclic voltammetry of 1.11 mM $[MoH_2(\eta^2\text{-}O_2CH)(dppe)_2][BPh_4]$ complex in 3:1 $[NBu_4][BF_4]$-Toluene at a vitreous carbon electrode at various scan rates at 303 K.

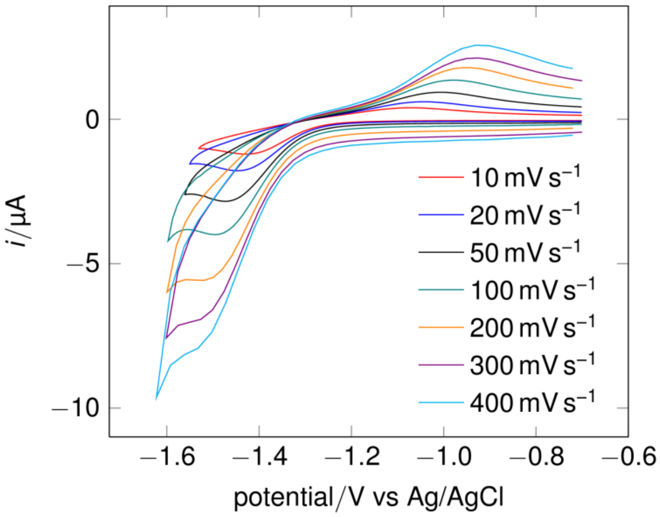

Figure A3.6 Cyclic voltammetry of 1.10 mM $[WH_2(\eta^2\text{-}O_2CCH_3)(dppe)_2][BPh_4]$ complex in 3:1 $[NBu_4][BF_4]$-Toluene at a vitreous carbon electrode at various scan rates at 303 K.

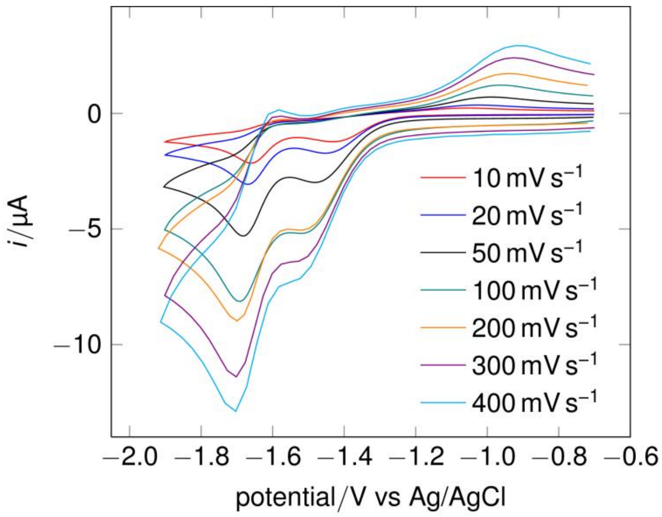

Figure A3.7 Cyclic voltammetry of 1.10 mM $[WH_2(\eta^2\text{-}O_2CCH_3)(dppe)_2][BPh_4]$ complex in 3:1 $[NBu_4][BF_4]$-Toluene at a vitreous carbon electrode at various scan rates at 303 K.

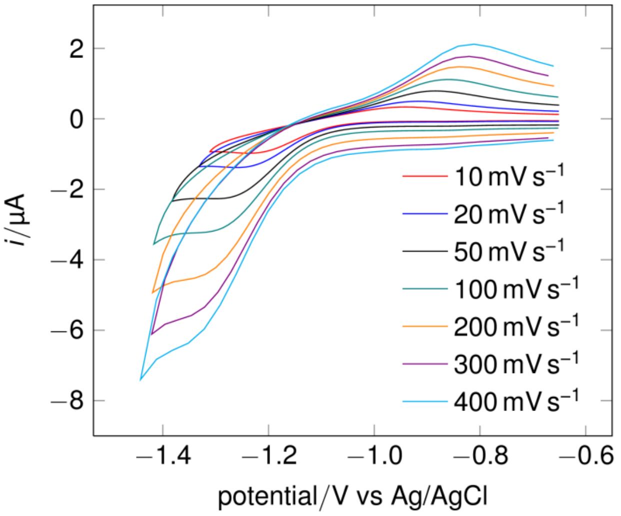

Figure A3.8 Cyclic voltammetry of 1.13 mM $[WH_2(\eta^2\text{-}O_2CH)(dppe)_2][BPh_4]$ complex in 3:1 $[NBu_4][BF_4]$-Toluene at a vitreous carbon electrode at various scan rates at 303 K.

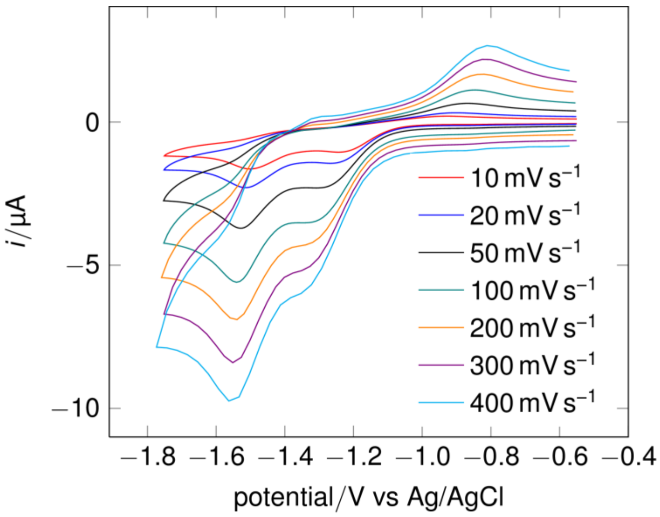

Figure A3.9 Cyclic voltammetry of 1.13 mM $[WH_2(\eta^2\text{-}O_2CH)(dppe)_2][BPh_4]$ complex in 3:1 $[NBu_4][BF_4]$-Toluene at a vitreous carbon electrode at various scan rates at 303 K.

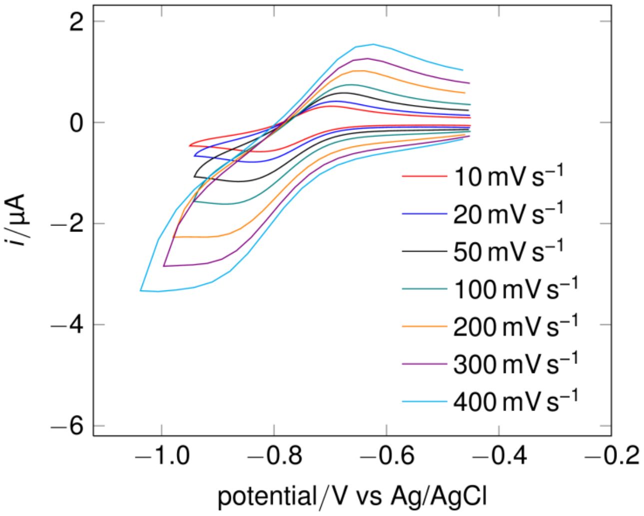

Figure A3.10 Cyclic voltammetry of 0.60 mM $[WH_2(\eta^2\text{-}O_2CCF_3)(dppe)_2][BPh_4]$ complex in 3:1 $[NBu_4][BF_4]$-Toluene at a vitreous carbon electrode at various scan rates at 303 K.

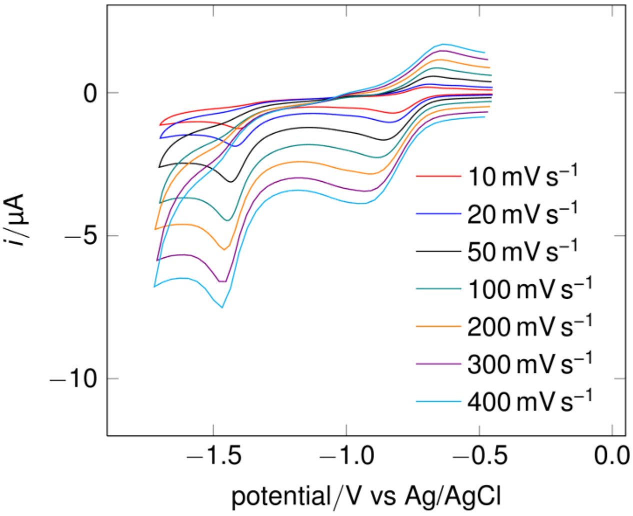

Figure A3.11 Cyclic voltammetry of 0.60 mM [$WH_2(\eta^2-O_2CCF_3)(dppe)_2$][$BPh_4$] complex in 3:1 [$NBu_4$][$BF_4$]-Toluene at a vitreous carbon electrode at various scan rates at 303 K.

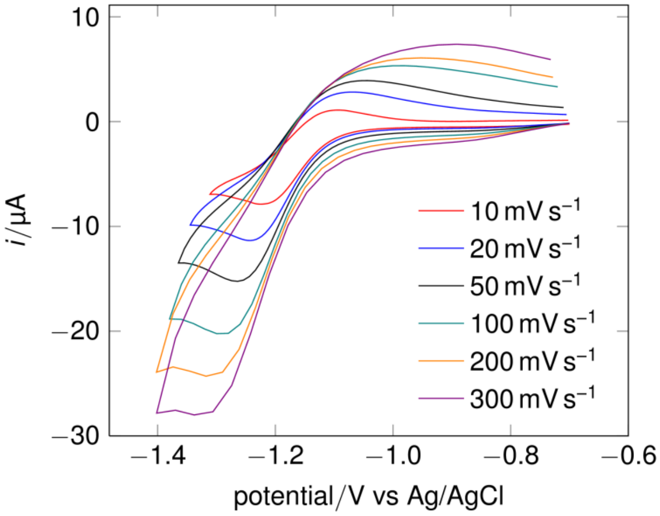

Figure A3.12 Cyclic voltammetry of 1.10 mM [$MoH_2(\eta^2-O_2CCH_3)(dppe)_2$][$BPh_4$] complex in 0.1 M [$NBu_4$][$BF_4$]-MeCN at a vitreous carbon electrode at various scan rates at 303 K.

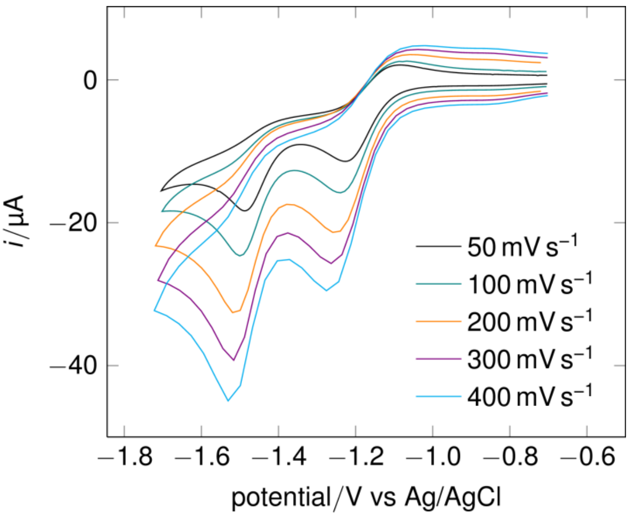

Figure A3.13 Cyclic voltammetry of 1.10 mM [$MoH_2(\eta^2-O_2CCH_3)(dppe)_2$][$BPh_4$] complex in 0.1 M [$NBu_4$][$BF_4$]-MeCN at a vitreous carbon electrode at various scan rates at 303 K.

Exp. No	Catalyst / µmols (Concentration / mM)	H^+ / µmols (Concentration / mM)	Charge passed / µmols e (Charge passed / C)	Yield H_2 / µmols	C. E. / %	C. Y. / %
1	2.98 (1.49)	17.88 (8.94)	10.57 (1.02)	3.96	74.92	16.6
2	5.89 (1.47)	88.35 (22.05)	17.83 (1.71)	8.24	92.45	17.5
3	5.97 (1.49)	53.73 (13.41)	19.69 (1.90)	8.28	84.09	27.7

Table A3.1 Controlled potential electrolysis data for $[MoH_2(\eta^2\text{-}O_2CCH_3)(dppe)_2][BPh_4]$ complex in 0.1 M $[NBu_4][BF_4]$-MeCN at a large vitreous carbon electrode in the presence of a low concentration of acid.

Chapter 4

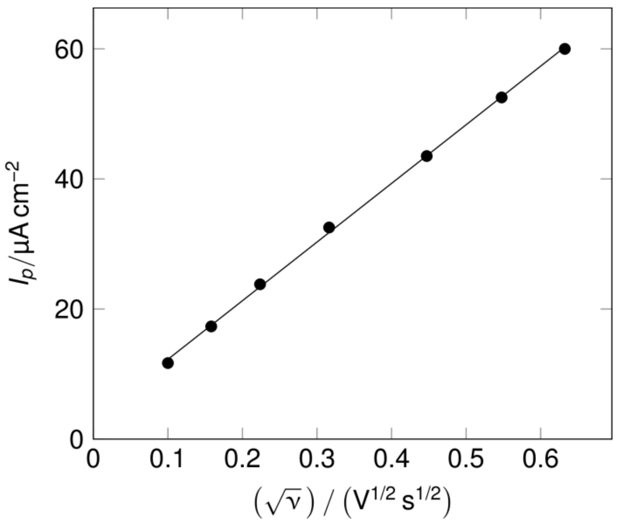

Figure A4.1 Plot of cathodic peak current *vs.* square root of scan rate for the first reduction of $[Mo(CO)_2(S_2C_2Ph_2)_2]$.

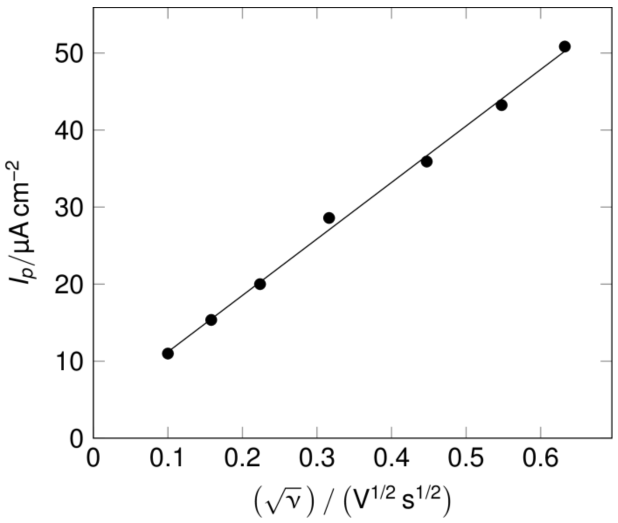

Figure A4.2 Plot of cathodic peak current *vs.* square root of scan rate for the second reduction of $[Mo(CO)_2(S_2C_2Ph_2)_2]$.

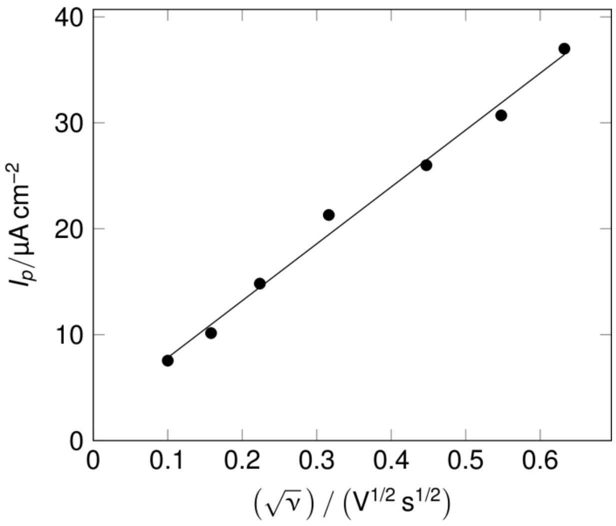

Figure A4.3 Plot of cathodic peak current *vs.* square root of scan rate for the first reduction of $[W(CO)_2(S_2C_2Ph_2)_2]$.

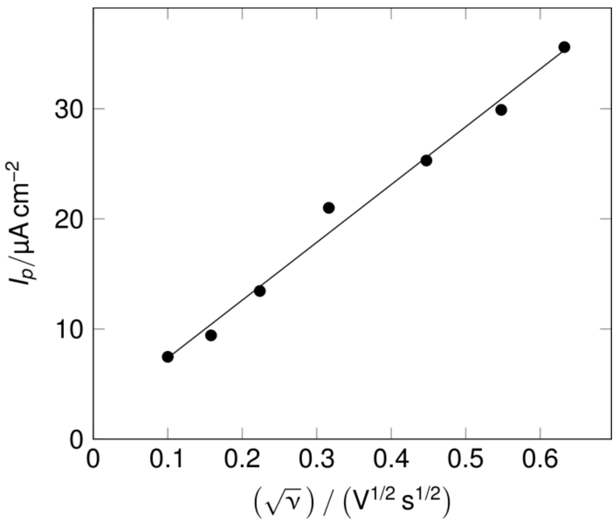

Figure A4.4 Plot of cathodic peak current *vs.* square root of scan rate for the second reduction of $[W(CO)_2(S_2C_2Ph_2)_2]$.

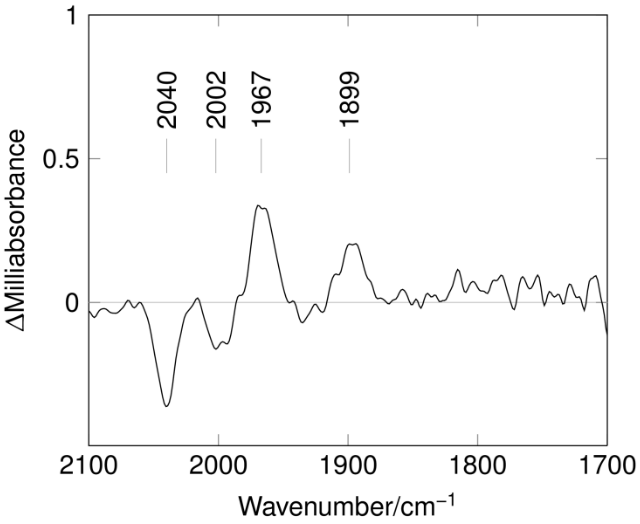

Figure A4.5 Difference spectrum for the first reduction ($M^{IV/III}$) of 9 mM $[Mo(CO)_2(S_2C_2Ph_2)_2]$ in 0.2 M $[Bu_4N]BF_4]$-DCM for a scan at 0.88 s relative to a scan at 0.08 s.

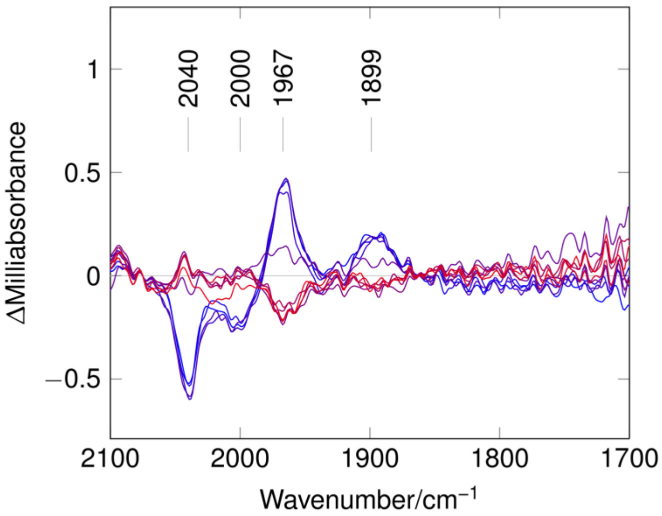

Figure A4.6 Difference spectrum for the first reduction ($M^{IV/III}$) of 9 mM $[Mo(CO)_2(S_2C_2Ph_2)_2]$ in 0.2 M $[Bu_4N]BF_4]$-DCM in the time range 0.34 s (blue) to 14.00 s (red) relative to a scan at 0.08 s.

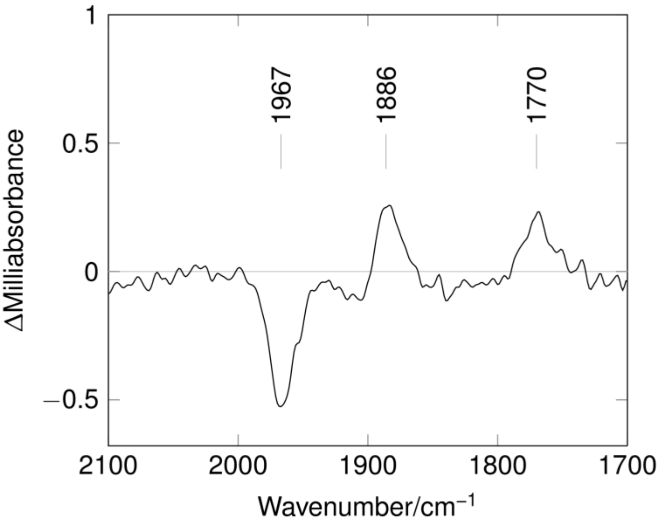

Figure A4.7 Difference spectrum for the second reduction ($M^{III/II}$) of 9 mM [$Mo(CO)_2(S_2C_2Ph_2)_2$] in 0.2 M [Bu_4N]BF_4]-DCM for a scan at 0.88 s relative to a scan at 0.08 s.

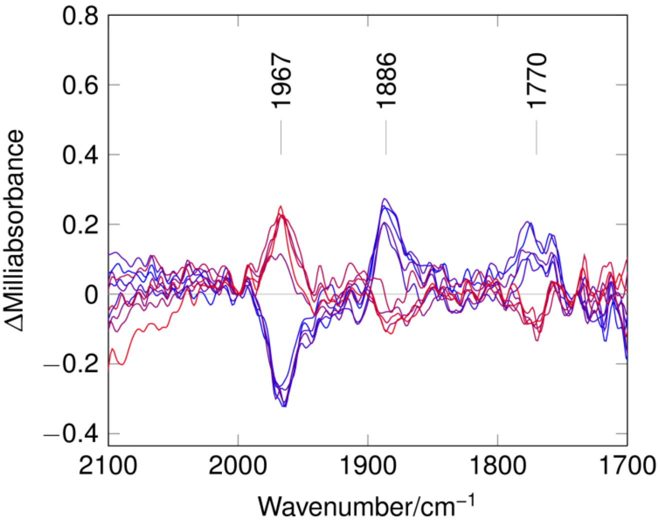

Figure A4.8 Difference spectrum for the second reduction ($M^{III/II}$) of 9 mM [$Mo(CO)_2(S_2C_2Ph_2)_2$] in 0.2 M [Bu_4N]BF_4]-DCM in the time range 0.34 s (blue) to 14.00 s (red) relative to a scan at 0.08 s.

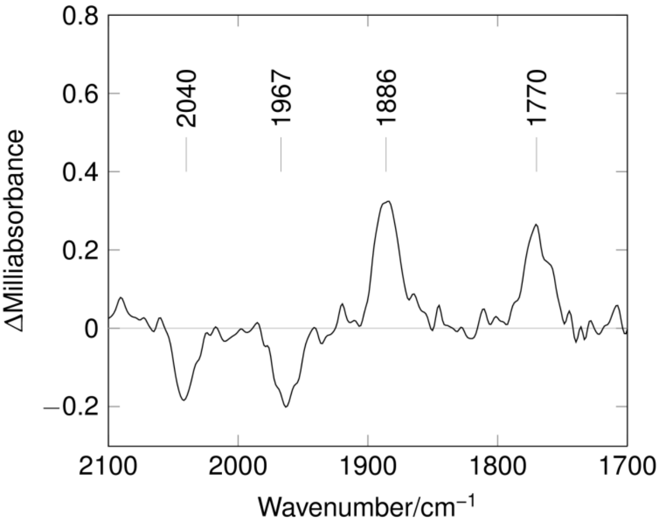

Figure A4.9 Difference spectrum for the direct second reduction ($M^{IV/II}$) of 9 mM $[Mo(CO)_2(S_2C_2Ph_2)_2]$ in 0.2 M $[Bu_4N]BF_4$]-DCM for a scan at 0.88 s relative to a scan at 0.08 s.

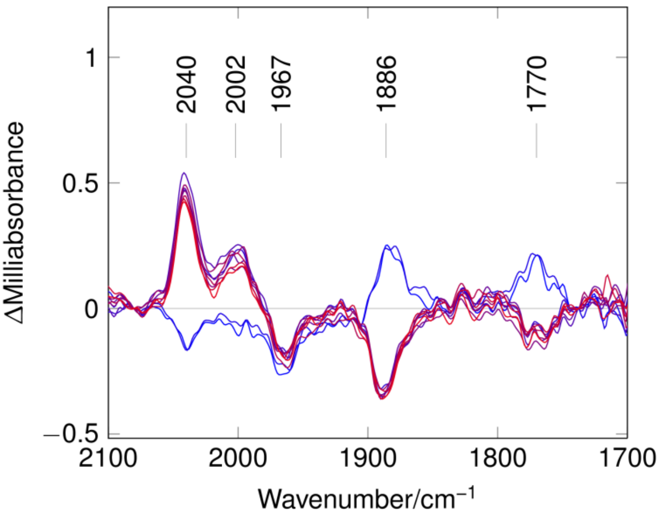

Figure A4.10 Difference spectrum for the direct second reduction ($M^{IV/II}$) of 9 mM $[Mo(CO)_2(S_2C_2Ph_2)_2]$ in 0.2 M $[Bu_4N]BF_4$]-DCM in the time range 0.34 s (blue) to 14.00 s (red) relative to a scan at 0.08 s.

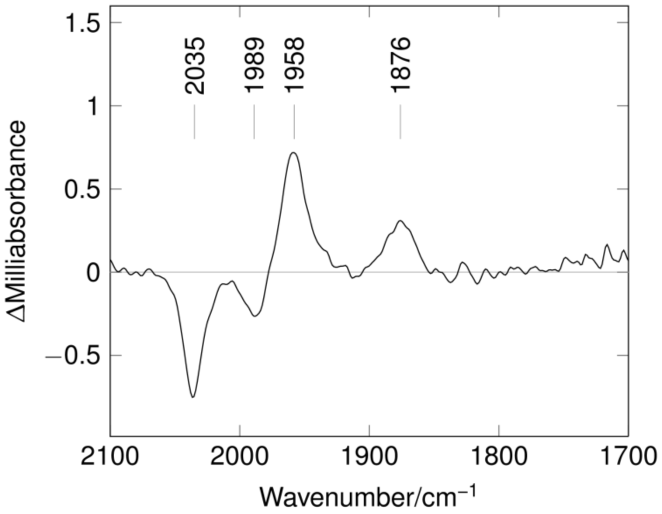

Figure A4.11 Difference spectrum for the first reduction ($M^{IV/III}$) of 9 mM $[W(CO)_2(S_2C_2Ph_2)_2]$ in 0.2 M $[Bu_4N]BF_4$-DCM for a scan at 0.88 s relative to a scan at 0.08 s.

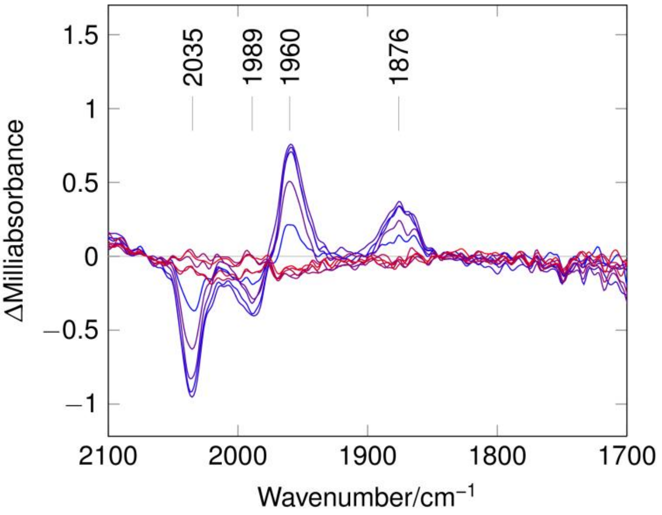

Figure A4.12 Difference spectrum for the first reduction ($M^{IV/III}$) of 9 mM $[W(CO)_2(S_2C_2Ph_2)_2]$ in 0.2 M $[Bu_4N]BF_4$-DCM in the time range 0.34 s (blue) to 14.00 s (red) relative to a scan at 0.08 s.

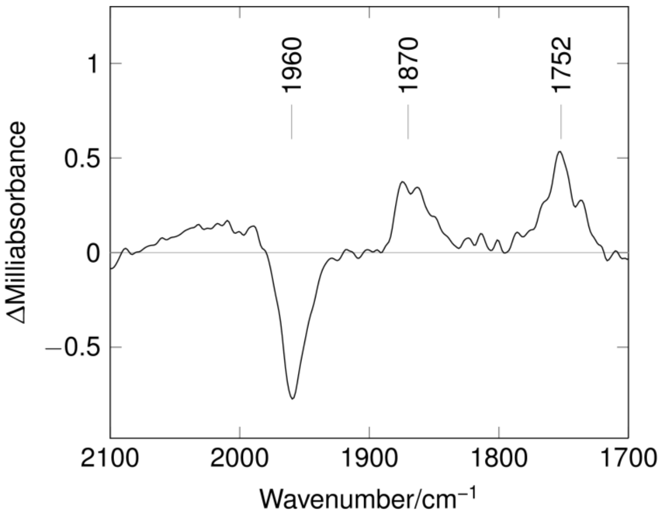

Figure A4.13 Difference spectrum for the second reduction ($M^{III/II}$) of 9 mM [$W(CO)_2(S_2C_2Ph_2)_2$] in 0.2 M [Bu_4N]BF_4-DCM for a scan at 0.88 s relative to a scan at 0.08 s.

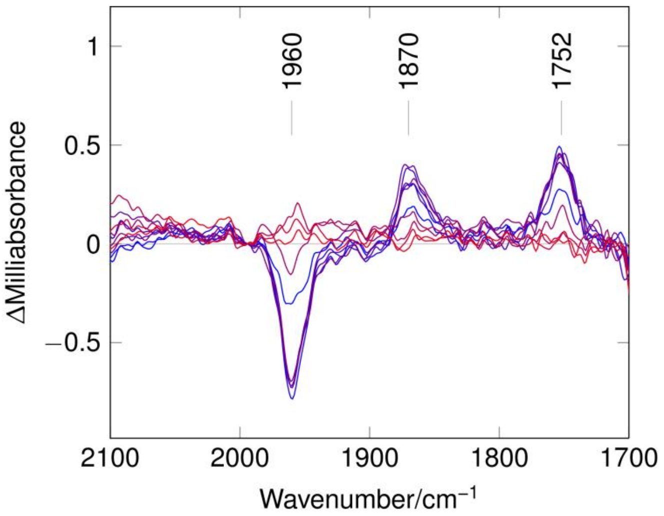

Figure A4.14 Difference spectrum for the second reduction ($M^{III/II}$) of 9 mM [$W(CO)_2(S_2C_2Ph_2)_2$] in 0.2 M [Bu_4N]BF_4-DCM in the time range 0.34 s (blue) to 14.00 s (red) relative to a scan at 0.08 s.

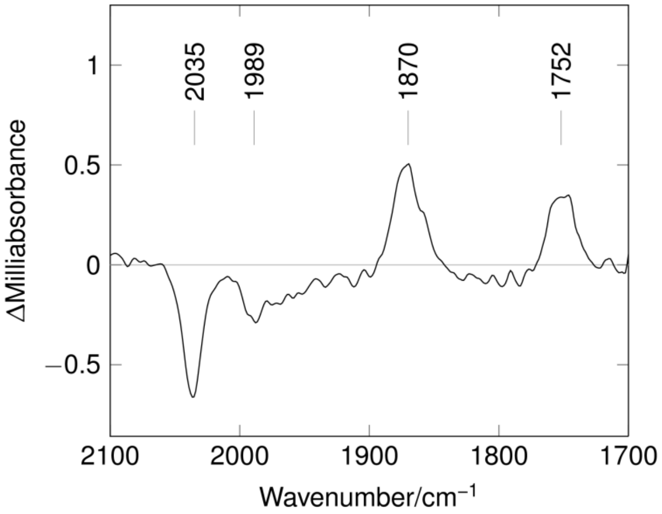

Figure A4.15 Difference spectrum for the direct second reduction ($M^{IV/II}$) of 9 mM [W(CO)$_2$(S$_2$C$_2$Ph$_2$)$_2$] in 0.2 M [Bu$_4$N]BF$_4$]-DCM for a scan at 0.88 s relative to a scan at 0.08 s.

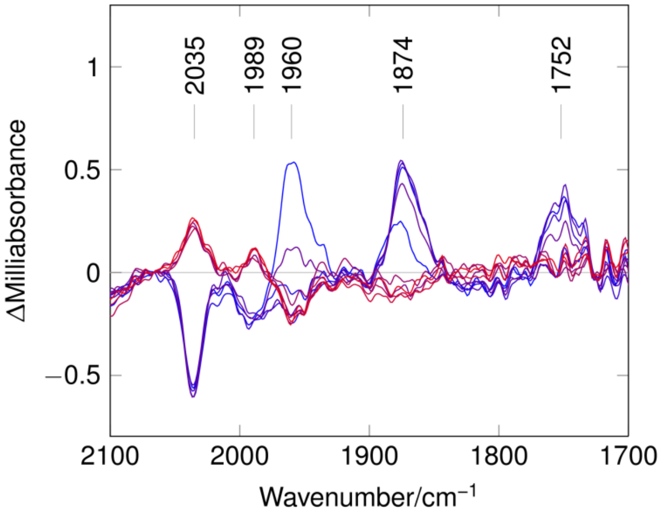

Figure A4.16 Difference spectrum for the direct second reduction ($M^{IV/II}$) of 9 mM [W(CO)$_2$(S$_2$C$_2$Ph$_2$)$_2$] in 0.2 M [Bu$_4$N]BF$_4$]-DCM in the time range 0.34 s (blue) to 14.00 s (red) relative to a scan at 0.08 s.

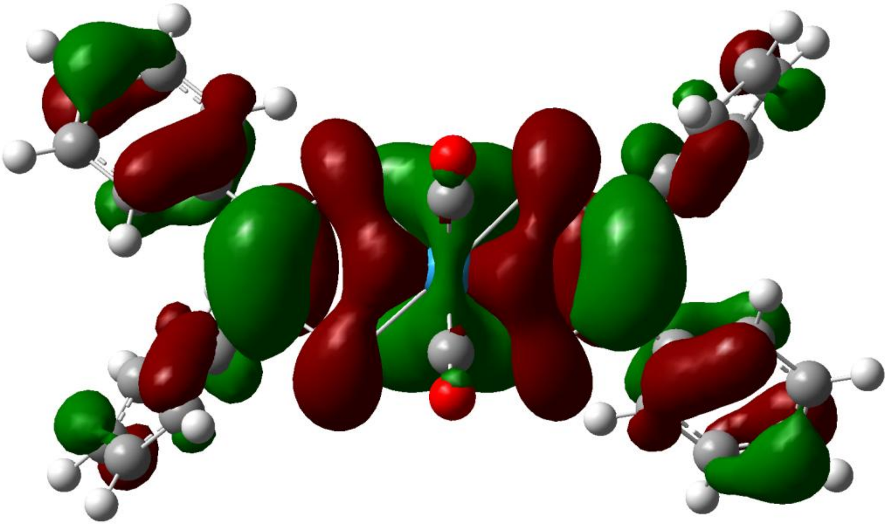

Figure A4.17 Electron distribution in the HOMO of $[W(CO)_2(S_2C_2Ph_2)_2]$.

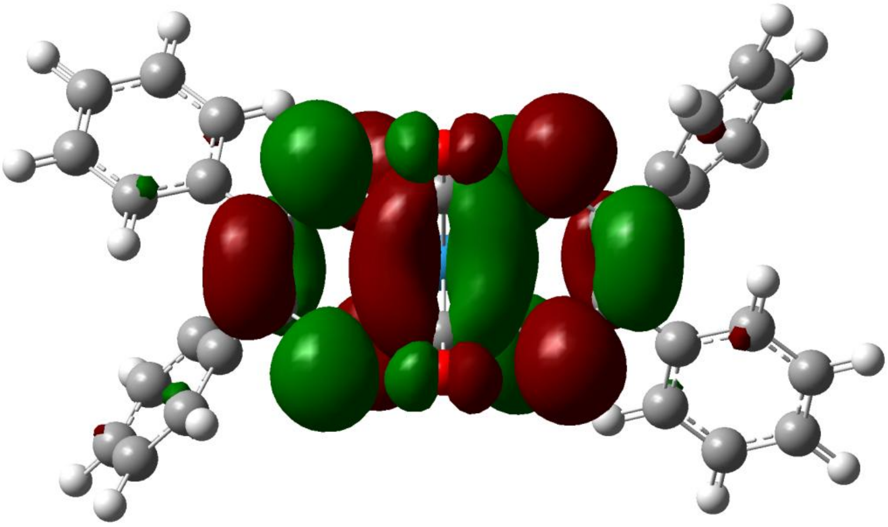

Figure A4.18 Electron distribution in the SOMO of $[W(CO)_2(S_2C_2Ph_2)_2]^-$.

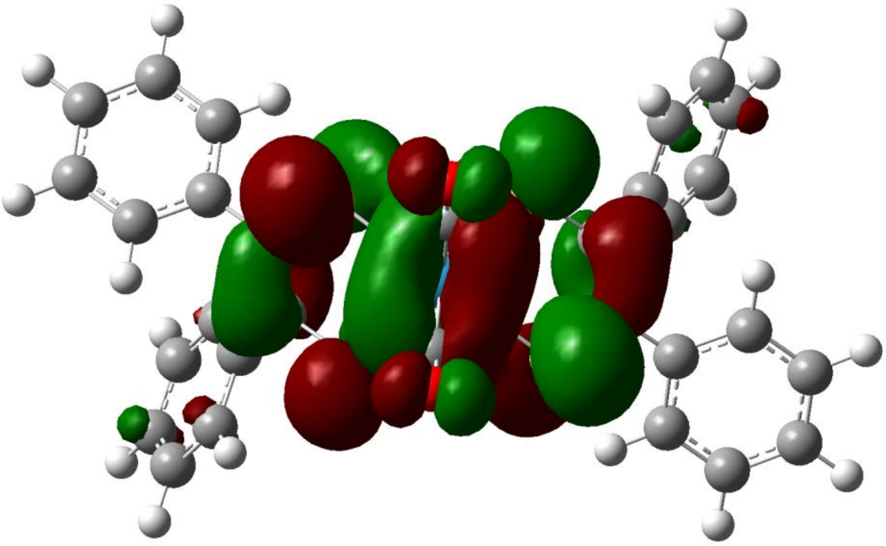

Figure A4.19 Electron distribution in the LUMO of $[W(CO)_2(S_2C_2Ph_2)_2]^{2-}$.

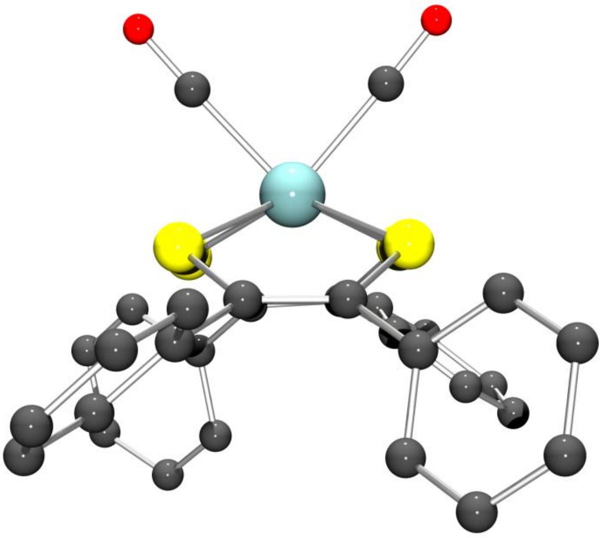

Figure A4.20 Structural representation of $[W(CO)_2(S_2C_2Ph_2)_2]$.

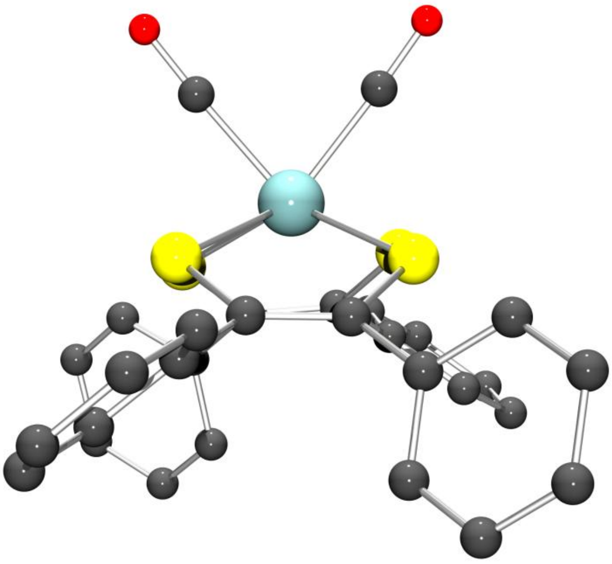

Figure A4.21 Structural representation of the one electron reduced, $[W(CO)_2(S_2C_2Ph_2)_2]^{1-}$.

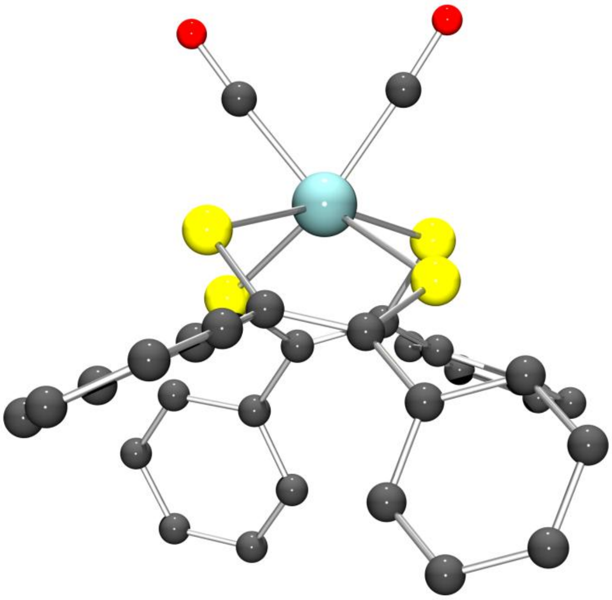

Figure A4.22 Structural representation of the two electron reduced, $[W(CO)_2(S_2C_2Ph_2)_2]^{2-}$.

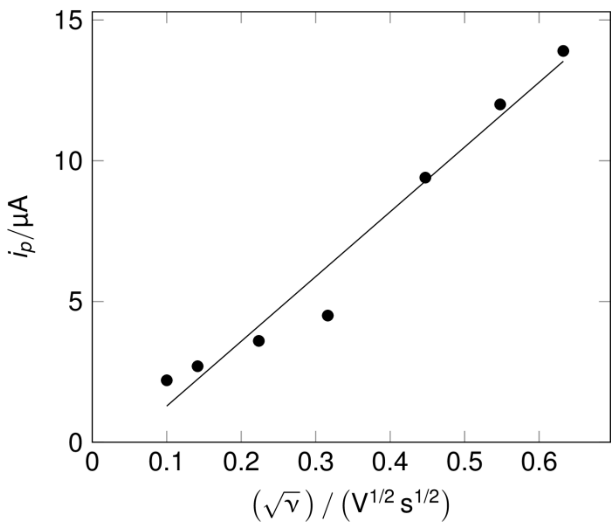

Figure A4.23 Plot of anodic peak current *vs* square root of scan rate for the first oxidation of $[Mo(CO)_2(S_2C_2Ph_2)_2]$.

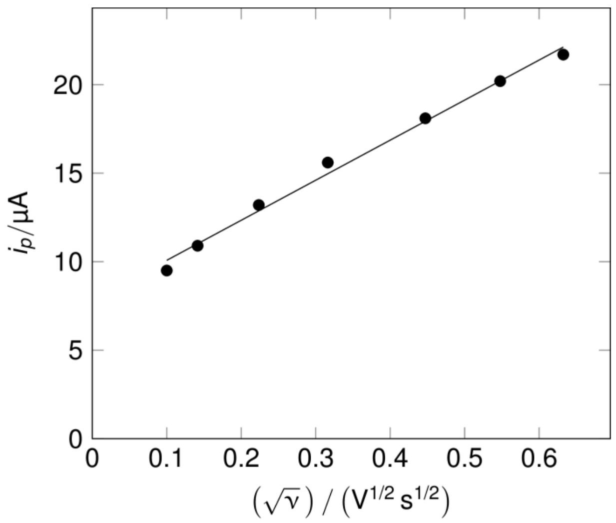

Figure A4.24 Plot of anodic peak current *vs* square root of scan rate for the second oxidation of $[Mo(CO)_2(S_2C_2Ph_2)_2]$.

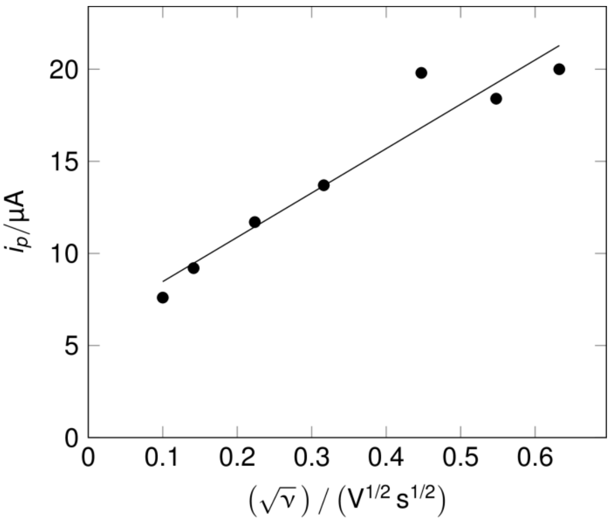

Figure A4.25 Plot of anodic peak current *vs* square root of scan rate for the first oxidation of $[W(CO)_2(S_2C_2Ph_2)_2]$.

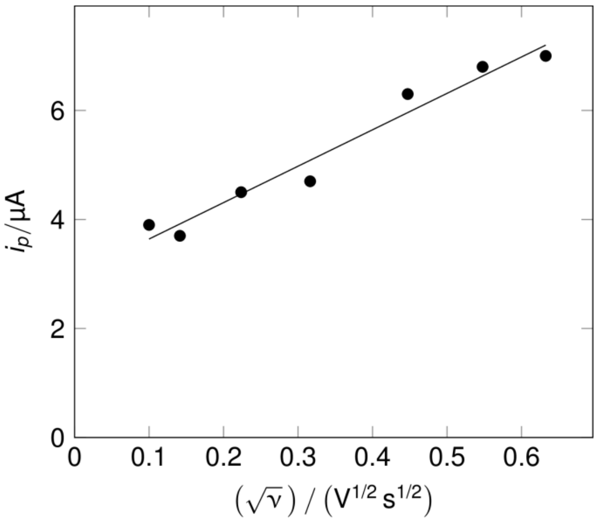

Figure A4.26 Plot of anodic peak current *vs* square root of scan rate for the second oxidation of $[W(CO)_2(S_2C_2Ph_2)_2]$.

Exp. No.	Solvent	Acid source	No. eq. acid	Complex / µmol (Concentration / mM)	H_2 / µmol	TON	No. e per mol of complex / F mol^{-1}	CE - 2e / %	CY / %
1	MeCN	Pyridinium	7	5.74 (2.86)	9.09	1.58	9.11	44.5	45.2
2	MeCN	Pyridinium	7	7.59 (3.80)	9.72	1.28	9.42	34.5	36.6
3	MeCN	Pyridinium	7	3.70 (1.85)	4.51	1.22	9.00	34.8	34.8
4	MeCN	Pyridinium	7	1.11 (0.58)	2.93	2.64	8.97	75.7	75.4
5	MeCN	Pyridinium	7	1.04 (0.52)	1.51	1.45	7.55	52.3	41.5
6	MeCN	Pyridinium	7	0.56 (0.28)	0.66	1.18	6.23	55.9	33.8
7	MeCN	Anilinium	6	0.28 (0.14)	0.51	1.81	8.50	55.8	60.5
8	DCM	Trifluoroacetic acid	5	0.59 (0.30)	1.02	1.73	7.07	68.2	69.2
9	DCM	Trifluoroacetic acid	6	0.56 (0.28)	0.19	0.34	4.77	24.3	11.2
10	DCM	Trifluoroacetic acid	6	0.56 (0.28)	0.35	0.62	6.70	26.2	20.5
11	DCM	Trifluoroacetic acid	6	0.56 (0.14)	0.33	0.59	5.89	30.2	19.6

Table A4.1 Controlled low potential electrolysis data for $[Mo(CO)_2(S_2C_2Ph_2)_2]$ performed at -1.0 V *vs* SCE (CE - 2e = current efficiency when the two electrons required for generation of the catalytic species are ignored).

Exp. No.	**Solvent**	**Acid source**	**No. eq. acid**	**Complex / µmol (Concentration / mM)**	**H2 / µmol**	**TON**	**No. e per mol of complex / F mol^{-1}**	**CE - 2e / %**
1	DCM	Trifluoroacetic acid	2000	0.59 (0.30)	1.03	1.75	15.5	22.6
2	DCM	Trifluoroacetic acid	2000	0.69 (0.35)	0.97	1.41	9.01	31.3

Table A4.2 Controlled high potential electrolysis data for $[Mo(CO)_2(S_2C_2Ph_2)_2]$ performed at -0.5 V *vs* SCE (CE - 2e = current efficiency when the two electrons required for generation of the catalytic species are ignored).

Exp. No	Solvent	Acid source	No. eq. acid	Complex / µmol (Concentration / mM)	H2 / µmol	TN	No. e per mol of complex / F mol^{-1}	CE - 2e / %	CY / %
1	DCM	Trifluoroacetic acid	5	0.54 (0.14)	0.22	0.40	4.61	30.9	16.1
2	DCM	Trifluoroacetic acid	5	0.89 (0.45)	0.38	0.43	4.07	41.5	17.2
3	DCM	Trifluoroacetic acid	6	0.78 (0.39)	0.98	1.26	8.08	41.3	41.8
4	DCM	Trifluoroacetic acid	6	0.78 (0.39)	0.19	0.24	3.41	34.4	8.08
5	DCM	Trifluoroacetic acid	8	0.78 (0.31)	0.12	0.15	8.64	4.56	3.78
6	DCM	Trifluoroacetic acid	9	0.35 (0.09)	1.12	3.20	17.8	40.6	71.1
7	DCM	Trifluoroacetic acid	10	0.78 (0.20)	0.41	0.52	4.99	34.9	10.4
8	DCM	Trifluoroacetic acid	9	0.86 (0.21)	0.42	0.49	4.73	35.9	10.9
9	DCM	Trifluoroacetic acid	9	0.65 (0.19)	0.40	0.62	3.54	80.0	13.7
10	DCM	Trifluoroacetic acid	7	0.48 (0.12)	0.65	1.35	6.92	54.7	38.5

Table A4.3 Controlled low potential electrolysis data for $[W(CO)_2(S_2C_2Ph_2)_2]$ performed at -1.1 V *vs* SCE (CE - 2e = current efficiency when the two electrons required for generation of the catalytic species are ignored).

Exp. No.	Solvent	Acid source	No. eq. acid	Complex / µmol (Concentration / mM)	H2 / µmol	TN	No. e per mol of complex / F mol^{-1}	CE - 2e / %
1	DCM	Trifluoroacetic acid	4000	0.67 (0.34)	2.51	3.75	30.3	24.7
2	DCM	Trifluoroacetic acid	4000	0.51 (0.26)	2.06	4.04	42.0	19.3

Table A4.4 Controlled high potential electrolysis data for $[W(CO)_2(S_2C_2Ph_2)_2]$ performed at -0.6 V vs SCE (CE - 2e = current efficiency when the two electrons required for generation of the catalytic species are ignored).

Chapter 5

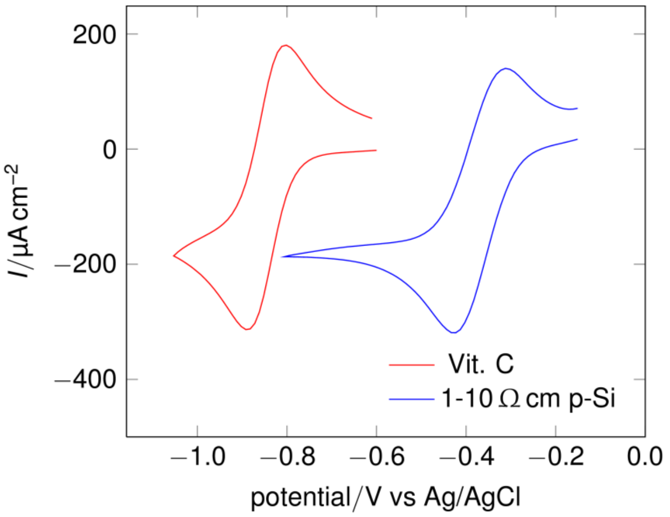

Figure A5.1 Cyclic voltammetry of 1.20 mM $[Cp_2Co][PF_6]$ complex in 0.1 M $[NBu_4][BF_4]$-MeCN at a vitreous carbon and p-type silicon electrodes showing the potential shift on the $[Cp_2Co]^+/[Cp_2Co]$ redox couple, $\Delta E_{½} = 0.47$ V.

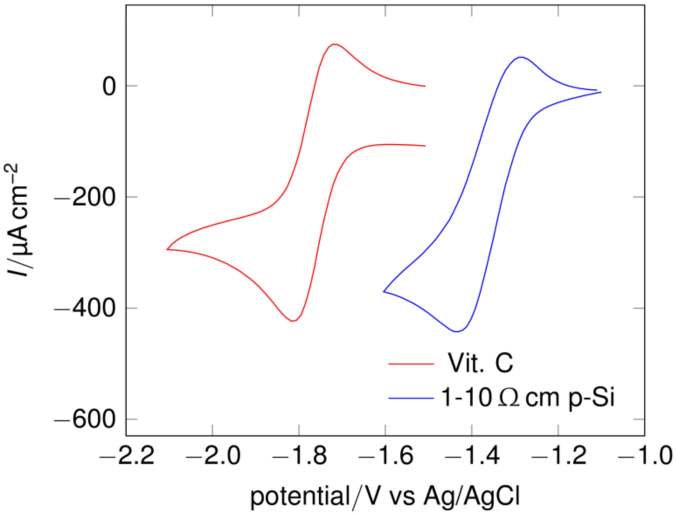

Figure A5.2 Cyclic voltammetry of 1.20 mM $[Cp_2Co][PF_6]$ complex in 0.1 M $[NBu_4][BF_4]$-MeCN at a vitreous carbon and p-type silicon electrodes showing the potential shift on the $[Cp_2Co]^+/[Cp_2Co]$ redox couple, $\Delta E_{½} = 0.41$ V.

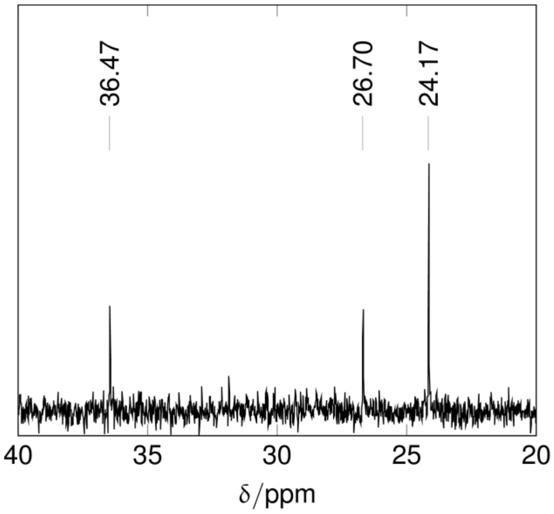

Figure A5.3 $^{31}P\{^{1}H\}$ NMR spectra of partial electrolysis (0.26 electrons per mol **A**) of *trans*-$[W(N_2H_2)(TsO)(dppe)_2]^+$ showing **A** at δ = 36.47 ppm and intermediates at δ = 26.70 and 24.17 ppm.

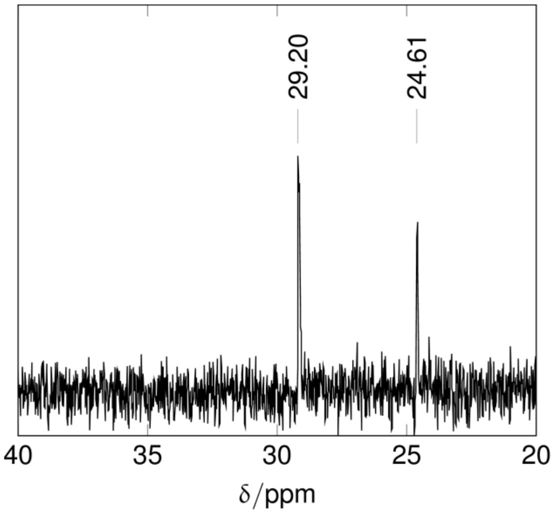

Figure A5.4 $^{31}P\{^{1}H\}$ NMR spectra of exhaustive electrolysis (3.00 electrons per mol **A**) of *trans*-$[W(N_2H_2)(TsO)(dppe)_2]^+$ showing intermediates at δ = 29.20 and 24.61 ppm.

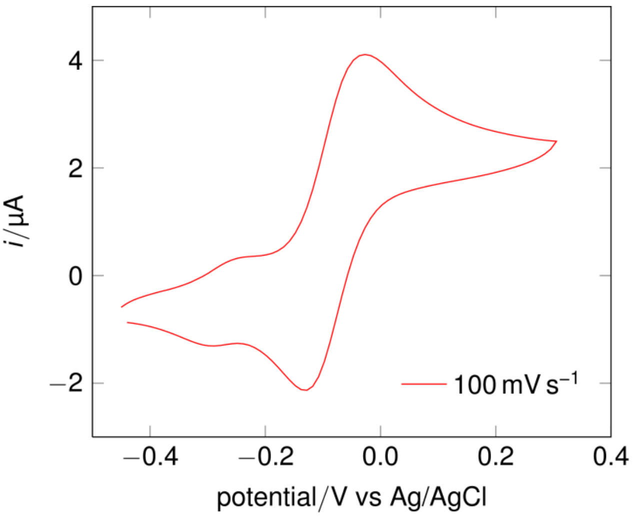

Figure A5.5 Cyclic voltammetry of *trans*-[$W(N_2)_2(dppe)_2$] in 0.2 M [NBu_4][BF_4]-THF at a vitreous carbon formed after electrolysis of *trans*-[$W(N_2H_2)(TsO)(dppe)_2$]$^+$.

Exp. No	A / µmol ([A] / mM)	No. electrons per mol A (Si) / F mol^{-1}	Mol % NH_3 per mol A (Si) / %	No. electrons per mol A (Hg) / F mol^{-1}	Mol % NH_3 per mol A (Hg) / %	Mol % B per mol A (Hg) / %
H1	5.98 (1.20)	0.28	49	0.99	5.5	13
H2	6.64 (1.33)	0.64	13	4.51	2.5	51
H3	6.64 (0.90)	1.64	22	2.40	1.6	67
H4	4.96 (1.06)	2.01	22	2.38	0.2	53

Table A5.1 Results of photo-assisted electrosynthesis of ammonia at an illuminated 1-10 Ω cm p-type Si electrode and then a dark Hg pool electrode in 0.2 M $[Bu_4N][BF_4]$-THF.